Physics of Fluids

RESEARCH ARTICLE | JUNE 22 2026

Floquet stability analysis of a circular cylinder on a viscoelastic support

Rahul Mishra ; Rajneesh Bhardwaj ; Mark C. Thompson

Check for updates

Physics of Fluids 38, 064122 (2026)
https://doi.org/10.1063/5.0326663

View Online
Export Citation

Articles You May Be Interested In

Floquet stability analysis of the wake of an inclined flat plate

Physics of Fluids (September 2013)

Floquet stability analysis in the wake of a NACA0015 airfoil at post-stall angles of attack

Physics of Fluids (September 2017)

The three-dimensional wake of a cylinder undergoing a combination of translational and rotational oscillation in a quiescent fluid

Physics of Fluids (June 2009)

22 June 2026 08:21:47

AIP Advances
Why Publish With Us?
21DAYS average time to 1st decision
OVER 4 MILLION views in the last year
INCLUSIVE scope
Learn More
AIP Publishing

AIP Publishing

Floquet stability analysis of a circular cylinder on a viscoelastic support

Cite as: Phys. Fluids **38**, 064122 (2026); doi: 10.1063/5.0326663
Submitted: 7 February 2026 · Accepted: 4 June 2026 ·
Published Online: 22 June 2026

View Online Export Citation CrossMark

Rahul Mishra,[1,a)] Rajneesh Bhardwaj,[2] and Mark C. Thompson[3]

AFFILIATIONS

[1]SR University, Warangal, Telangana 506371, India
[2]Department of Mechanical Engineering, IIT Bombay, Mumbai, Maharashtra 400076, India
[3]Fluids Laboratory for Aeronautical and Industrial Research (FLAIR), Department of Mechanical and Aerospace Engineering, Monash University, Clayton 3800, Australia

[a)]Author to whom correspondence should be addressed: rahulmishra.iitk@gmail.com

ABSTRACT

A numerical stability analysis of the wake of a circular cylinder undergoing vortex-induced vibration (VIV) subject to viscoelastic support is presented. For this structural setup, the arrangement of the springs and damper is similar to that for the standard linear solid (SLS) model used to model a viscoelastic material. The SLS system is governed by two parameters: (a) the ratio of the linear spring constants, R, and (b) the damping ratio, ζ. All simulations are done for $R = 1$, but covering $\zeta = 0, 0.001, 1$, and 10. Stability is investigated for the reduced velocity range over which there is a strong resonant response: $U_r = [4.5, 8]$, and for a mass ratio of $m^* = 2.546$. The dominant instability modes present are analogous to modes A, B, and QP (quasi-periodic) observed for a stationary circular cylinder wake, except at $U_r = 4.5$, which shows modes B, QP, and a subharmonic mode, SH. The critical Reynolds number for two- to three-dimensional transition is observed to decrease with an increase of U_r. In this resonant range, for both the standard spring–damper system and the SLS-based VIV model, the critical Reynolds number below which two-dimensional simulations remain valid is $\mathrm{Re}_{cr} \approx 212$, with transition first occurring at $U_r = 8$ for a critical spanwise wavelength $\lambda_{cr} \approx 4.0D$. The results can be employed for setting Reynolds-number/reduced-velocity limits on two-dimensional numerical investigations of VIV under viscoelastic support.

Published under an exclusive license by AIP Publishing. https://doi.org/10.1063/5.0326663

22 June 2026 08:21:47

I. INTRODUCTION

Vortex-induced vibrations have been rigorously studied owing to their critical role in a broad range of applications spanning aerospace, civil, mechanical, offshore, and nuclear-reactor engineering (Sarpkaya, 1979; Bearman, 1984; Parkinson, 1989; Sarpkaya, 2004; Williamson and Govardhan, 2004; 2008; Bearman, 2011; Wu *et al.*, 2012; Soti *et al.*, 2018; Eswaran *et al.*, 2025; and Zhao *et al.*, 2024). Numerous two-dimensional numerical investigations of vortex-induced vibration (VIV) at low Reynolds numbers have been performed under the assumption that the wake remains strictly two-dimensional. This assumption is partially justified as the transverse oscillation of the cylinder can delay the onset of three-dimensional wake instability. However, post-transition, the development of three-dimensional flow structures can substantially alter the resulting VIV dynamics. Therefore, it is crucial to establish the Reynolds-number regime within which two-dimensional modeling provides a physically reliable representation of the flow.

While the delay in the onset of three-dimensionality in the flow past an elastically mounted circular cylinder undergoing vortex-induced vibration has been examined in our previous study (Mishra *et al.*, 2024), the primary objective of this paper is to assess how transverse oscillations influence 3D wake transition for a circular cylinder supported by a viscoelastic mounting modeled as a standard linear solid (SLS) system.

The SLS model represents a nonstandard elastic support configuration, as illustrated in Fig. 1, consisting of two springs and a damper. Here, k and k_n represent the non-equilibrium and equilibrium stiffness of the spring, respectively, while c denotes the damping coefficient. The SLS system provides a more generalized viscoelastic representation than the conventional spring–damper (Kelvin–Voigt) configuration. Unlike the Kelvin–Voigt model, where vibration amplitude decreases monotonically with damping, the SLS system enables a dynamic response due to the interaction of equilibrium and non-equilibrium stiffness. This additional tunability makes the SLS configuration particularly relevant for applications requiring either suppression of vortex-induced vibrations or enhancement of vibration amplitudes for energy harvesting purposes (Mishra *et al.*, 2020). The SLS framework can be employed in fluid–structure interaction

Published under an exclusive license by AIP Publishing

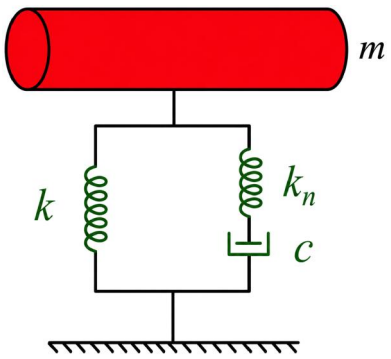


FIG. 1. Schematic of spring + spring–damper arrangement representing the SLS model used in the present study.

and compliant wall studies due to its ability to represent viscoelastic effects with a limited number of material parameters while maintaining computational efficiency and numerical stability (Mishra *et al.*, 2019).

As a reference case, flow past a stationary cylinder is considered, for which the transition from the 2D Kármán vortex street to a 3D wake as Reynolds number is increased is well established. In this regime, two dominant instability modes characterize the onset of three-dimensionality, commonly referred to as mode A and mode B. Stability analyses indicate that the first three-dimensional instability, mode A, appears at a critical Reynolds number of approximately $Re \approx 190$. This mode features a spanwise-periodic structure with a characteristic wavelength $\lambda \approx 4D$ where D is the diameter of cylinder (Barkley and Henderson, 1996; Williamson, 1996). A second instability, mode B, is predicted by Floquet stability analysis to occur at $Re \approx 260$, with $\lambda \approx 0.8D$ (Barkley and Henderson, 1996).

Floquet stability analysis reveals the existence of another theoretically admissible three-dimensional instability in the circular cylinder wake, namely a quasi-periodic (QP) mode. This mode is characterized by a complex-conjugate pair of Floquet multipliers, which together give rise to either traveling or standing wave structures (Blackburn and Lopez, 2003). The presence of complex-conjugate multipliers indicates that the temporal frequencies of the perturbation and the base flow period are incommensurate. For the stationary circular cylinder wake, Floquet analysis predicts that the QP mode becomes unstable at a critical Reynolds number of approximately $Re \approx 377$. Above the threshold, the QP mode is unstable over an intermediate spanwise wavelength range of $1.5D - 2D$.

The physical mechanisms governing mode A and mode B instabilities are fundamentally distinct. Williamson (1996) attributed the mode A instability to an elliptic instability of the vortex cores, whereas mode B was linked to an instability originating in the braid region (Leweke and Williamson, 1998). For the case where the body geometry is not mirror-symmetric across the streamwise centerline, a third (subharmonic) mode, mode C, is triggered. The mode structure shows characteristics of both modes A and B (Sheard *et al.*, 2005). These and related studies were done primarily for cylindrical bodies, either fixed or under forced oscillation. They focused on finding the dominant three-dimensional modes, the effect of Reynolds number, Re, and amplitude of oscillation, A^*, on these modes, and the effect of loss of spatio-temporal symmetry of the base flow. Recently, Mishra *et al.* (2024) investigated the transition of flow past an elastically mounted circular cylinder and identified the critical Reynolds number for 2D to 3D transition in a vortex-induced vibration (VIV) system using Floquet analysis based on high-fidelity numerical simulations.

However, recent studies by Mishra *et al.* (2019) on the *standard linear solid model* (SLS) of viscoelasticity motivated us to use the two springs and damper system as shown in Fig. 1 to investigate the effect on wake instabilities. The standard linear solid (SLS) system is a non-standard elastic mounting system. The VIV of an SLS system was investigated by Mishra *et al.* (2020). It was demonstrated that the SLS spring–damper system behaves similarly to the parallel spring–damper system up to a critical damping ratio (ζ_c). However, on a further increase of the damping ratio, the amplitude response actually increases. The non-monotonic vibration amplitude response with damping ratio can be presented in a "Griffin Plot" (see, e.g., Mishra *et al.*, 2020). Typically, in those studies, the Reynolds number was chosen to be low enough to ensure a two-dimensional wake. The question arises as to the Reynolds number limit to ensure the wake remains two-dimensional. To the knowledge of the authors, the Floquet stability analysis of an SLS spring–damper system at low mass ratios has received little or no attention in the literature, yet it provides an effective means of tuning the amplitude response. The variation of amplitude and possibly flow state, in turn, affects the critical Re for different modes (Leontini *et al.*, 2007) and hence transitions to three-dimensional flow. The primary motivation for this study is to determine the Re limits of two-dimensional VIV simulations for the SLS system, and, in particular, whether changes to the standard von Kármán wake state strongly affect the stability. Mishra *et al.* (2024) showed that, for a standard spring–damper VIV system at $\mathrm{Re} = 300$, increasing reduced velocity leads to 3D transition through different instability modes. These mode transitions govern vibration amplitude and wake three-dimensionality, demonstrating strong coupling between reduced velocity and flow instability mechanisms. The present work extends this framework to the SLS system, examining how these mode-transition characteristics are modified under the proposed SLS structural configuration.

The layout of this paper is as follows. In Sec. II, the theoretical background of the Floquet stability analysis is presented, together with a brief description of the numerical methodology used to solve the coupled system. A grid-resolution study is performed at $Re = 300$ to ensure adequate numerical accuracy. Simulations at $Re = 305$ and $Re = 277$ are conducted to facilitate comparison with established benchmark results. The simulation results are presented in Sec. III for both undamped VIV and SLS model VIV. Wake instabilities and the corresponding instability modes are analyzed at $Re = 260$, 280, and 300. The three-dimensional transition is further investigated at $Re = 300$. Furthermore, the response of the undamped VIV system is compared with that of the SLS model as a function of reduced velocity. Finally, the critical Reynolds number for both undamped VIV and SLS model VIV wakes is examined as a function of reduced velocity.

II. METHODOLOGY

A. The spectral-element method

The fluid flow is modeled in the moving reference frame attached to the cylinder so that remeshing is not required (Rajamuni *et al.*, 2018; Leontini *et al.*, 2006). The governing equations are then

22 June 2026 08:21:47

Published under an exclusive license by AIP Publishing

the non-dimensional Navier–Stokes equations in an accelerated frame-of-reference,

$$\frac{\partial \mathbf{u}}{\partial t} = -(\mathbf{u}\cdot\nabla)\mathbf{u} - \nabla p + \frac{1}{Re}(\nabla^2\mathbf{u}) - \mathbf{a}, \tag{1}$$

and

$$\nabla\cdot\mathbf{u} = 0, \tag{2}$$

where $\mathbf{u}$ and p are the fluid velocity and kinematic pressure, respectively, and $\mathbf{a}$ is the acceleration of the reference frame attached to the cylinder, $\mathbf{a} = \frac{d\mathbf{u}_{cyl}}{dt}$, where $\mathbf{u}_{cyl}$ is the cylinder velocity vector.

These equations, together with the linear stability equations discussed below, are discretized using the spectral-element method (Karniadakis and Sherwin, 2013) using boundary-conforming four-sided elements. Internally, within each element, the fields are represented using tensor-product Lagrange polynomial expansions with Gauss–Legendre–Lobatto quadrature points as the interpolation points. This latter choice allows efficient evaluation of integrals that occur when applying the weighted residual method to determine the discrete equations for the velocity components and pressure at each node point. Importantly, the choice of element polynomial order can be made at runtime, which enables the effect of spatial resolution to be assessed without rebuilding the (macro-element) mesh. More details are provided in Thompson *et al.* (1996; 2006), Ryan *et al.* (2005), and Karniadakis and Sherwin (2013), amongst others.

The spatially discretized equations are discretized in time using a three-step time-splitting method, which accumulates the effects of convection, pressure/continuity, and diffusion terms on the velocity and pressure fields sequentially over each timestep. The third-order Adams–Bashforth scheme is used for the convection substep, and the θ-variation of the Crank–Nicholson scheme is used for the diffusion substep. The pressure substep is used to satisfy continuity of the velocity field as well as to update the pressure field. High-order pressure boundary conditions are employed (Karniadakis *et al.*, 1991) to satisfy mass conservation at no-slip surfaces. Further details can be found in Thompson *et al.* (1996; 2006), Rajamuni *et al.* (2018).

The governing dimensionless structural equation, which provides the acceleration of the cylinder, is given by (Mishra *et al.*, 2020)

$$\dddot{Y}^* + \frac{R\pi f^*}{\zeta}\ddot{Y}^* + 4\pi^2 f_n^{*2}(R+1)\dot{Y}^* + \frac{4\pi^3 R f^{*3}}{\zeta}Y^* = \frac{2Rf^*}{\zeta m^*}C_L + \frac{2}{\pi m^*}\dot{C}_L. \tag{3}$$

Here, $\dddot{Y}^* = \dddot{y}D/U^2$, $\ddot{Y}^* = \ddot{y}D/U^2$, $\dot{Y}^* = \dot{y}/U$, $Y^* = y/D$, and $C_L = F_y/\left(\frac{1}{2}\rho_f U^2 DL\right)$ correspond to the non-dimensional jerk, acceleration, velocity, displacement, and lift force, respectively. Here, ρ_f is the fluid density, $R = k_n/k$ is the stiffness ratio, and $\zeta = c/2\sqrt{km}$ is the damping ratio. L represents the spanwise length of the cylinder and is taken as 1. Additionally, $f^* = Df_n/U$ is the non-dimensional natural frequency of the system in a vacuum ($f_n = \frac{1}{2\pi}\sqrt{k/m}$), and $m^* = \rho_c/\rho_f$ is the mass ratio, with ρ_c the cylinder density. The oscillation response is recorded as a function of the reduced velocity, $U_r = 1/f^*$. This structural equation is solved in a coupled manner with the fluid equations using the methodology outlined by Rajamuni *et al.* (2018). Predictions of the VIV response for the SLS system using the coupled fluid/structural solver are presented in Mishra *et al.* (2020).

B. Floquet stability analysis

Floquet stability analysis is a method to determine the linear stability of the periodic wake to three-dimensional perturbations. In this analysis, the growth of linear perturbations is evaluated with respect to a pre-calculated periodic base flow. We consider a periodic two-dimensional wake (base-flow) $\mathbf{U}(x,y,t)$ with period T, and analyze its stability with respect to an infinitesimal three-dimensional perturbation $\mathbf{u}'(x,y,z,t)$. The equations that governs the perturbation field are obtained by substituting $\mathbf{U}(x,y,t) + \mathbf{u}'(x,y,z,t)$ for $\mathbf{u}(x,y,z,t)$; $p(x,y,t) + p'(x,y,z,t)$ for p, in Equation (1). The governing equations for perturbation growth are obtained by linearizing to give

$$\frac{\partial \mathbf{u}'}{\partial t} = -(\mathbf{U}.\nabla)\mathbf{u}' - (\mathbf{u}'.\nabla)\mathbf{U} - \nabla p' + \frac{1}{Re}(\nabla^2\mathbf{u}'), \tag{4}$$

and

$$\nabla.\mathbf{u}' = 0. \tag{5}$$

These equations are simplified by expressing the solution as a Fourier series expansion in the spanwise direction, z. The individual Fourier terms decouple so that the analysis can be done for each Fourier mode (i.e., spanwise wavelength) individually. In effect, this step reduces the three-dimensional problem to a set of two-dimensional problems for each spanwise wavelength in the same form as for the base flow field. These equations are not explicitly further reduced to the form of an eigenvalue problem for the time variation of a set of instability modes, but rather the growth or decay of perturbations for each selected spatial wavelength is determined by integrating the equations forward in time starting from a white noise field. After integrating through a number of periods to reduce the amplitude of all but the fastest growing/slowest decaying modes, successive perturbation fields are then stored at the end of subsequent baseflow periods. This set forms a Krylov subspace containing the dominant instability modes for each spanwise wavelength, which can be extracted using Arnoldi decomposition, as described in more detail in Barkley and Henderson (1996).

Thus, the main aim of the Floquet analysis is to determine the amplitude multiplier (μ) from one cycle to the next for the dominant instability mode at each spanwise wavelength tested. The approach and implementation of the method has been validated for a number of similar stability problems, e.g., Ryan *et al.* (2005), Rao *et al.* (2015), Leontini *et al.* (2007), and Mishra *et al.* (2024).

For the stability analysis conducted in this work, the discretized fluid Eqs. (1) and (2) and the fully coupled structural Eq. (3) are integrated in time until a periodic steady state is attained. Once periodicity is established, the velocity field is sampled at discrete intervals—typically 50–100 snapshots over one complete cycle. Quadratic interpolation of these stored fields is subsequently employed to provide the baseflow velocity field at each timestep required by the time-integration of the linear stability Eqs. (4) and (5).

C. Boundary conditions

The boundary conditions are shown in Fig. 2 and are described as follows. The fluid velocity is prescribed at the inlet, top, and bottom

22 June 2026 08:21:47

Published under an exclusive license by AIP Publishing

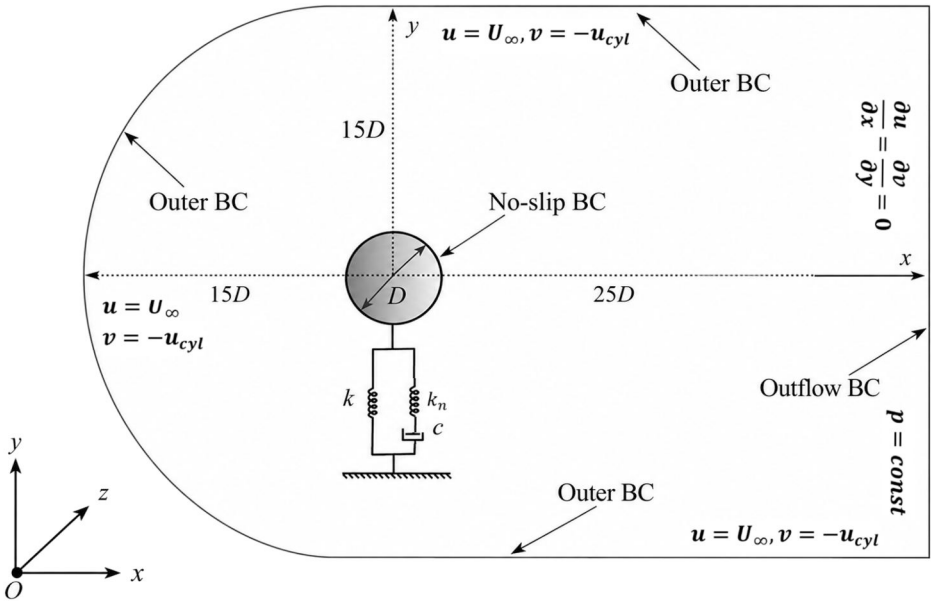


FIG. 2. Schematic of the computational domain and the boundary conditions for Floquet analysis.

boundaries and is given by $(U, V) = U_\infty \mathrm{i} - u_{cyl}\mathrm{j}$. The perturbation velocity components at these far-field boundaries are $u' = v' = w' = 0$, where u', v', and w' are the x, y, and z perturbation velocity components, respectively. At the surface of the cylinder, the no-slip condition is imposed, i.e., $(U, V) = 0$ and $(u', v', w') = 0$. At the outlet, the boundary condition is the same as the base flow condition, i.e., the normal velocity gradient is set to zero for both the base and perturbation velocity fields, and the pressure is fixed. At no-slip boundaries and at the far-field boundaries, higher-order boundary conditions are used for the normal pressure gradient for both the base and perturbation pressure, as described in Karniadakis *et al.* (1991).

D. Resolution studies

The spectral-element formulation employed in the present study has been rigorously validated in numerous prior investigations (Hourigan *et al.*, 2001; Sheard *et al.*, 2003; Rao *et al.*, 2015; Leontini *et al.*, 2007; and references therein). For the base flow simulations, the computational domain and element distribution were adopted from earlier studies on vortex-induced vibration (VIV) of a circular cylinder, wherein comprehensive resolution and validation analyses were reported (Mishra *et al.*, 2020). For the stability analysis, the mesh was constructed to ensure adequate spatial resolution, based on the resolution requirements established for the base flow. However, perturbation fields can exhibit smaller length scales than the base flow—especially at reduced spanwise wavelengths, so we investigated the convergence with respect to the polynomial order of the tensor-product intra-element interpolating polynomials. Three sets of element resolutions, 6×6, 8×8, and 10×10 for a parameter set that leads to near-maximal displacement: $Re = 300, \zeta = 0.0$, and oscillation frequency $f^* = 0.2$, have been used. As illustrated in Fig. 3, increasing the polynomial order from 7 (8×8) to 9 (10×10) changed the value of the Floquet multiplier less than 0.2% over the range of spanwise wavelengths investigated, providing confidence that the results presented herein are sufficiently resolved.

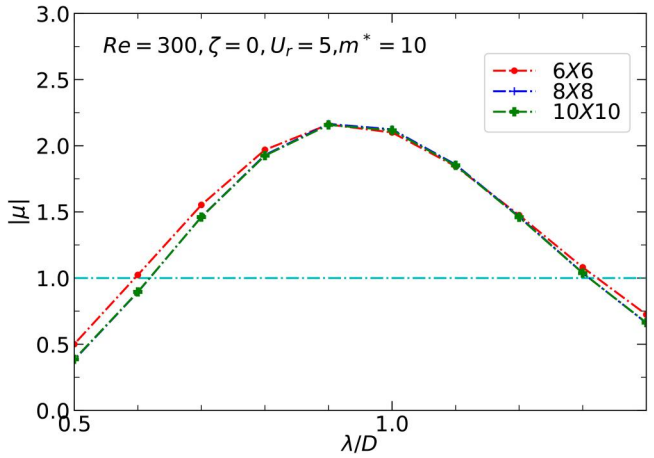


FIG. 3. Floquet multiplier, $|\mu|$, vs spanwise wavelength, λ/D, of Floquet modes as a function of number of nodes per spectral-element, for a cylinder undergoing VIV at $Re = 300, \zeta = 0.0$, and $f^* = 0.2$. This indicated that convergence is achieved for $n \times n = 8 \times 8$, corresponding to seventh order interpolating polynomials within elements.

E. Validation

A validation study was undertaken to verify that the produced results are consistent with previously published results for standard test cases. A comparison of the base flow VIV predictions for the present configuration against published literature results was reported in Mishra *et al.* (2021). Validation of the stability of the base flow under VIV is through a comparison against forced oscillation predictions of Leontini *et al.* (2007) for a standard spring–damper setup. Leontini *et al.* (2007) presented a transition map showing where different Floquet modes become unstable as a function of forced oscillation amplitude and Reynolds number. For the current problem, the

22 June 2026 08:21:47

Published under an exclusive license by AIP Publishing

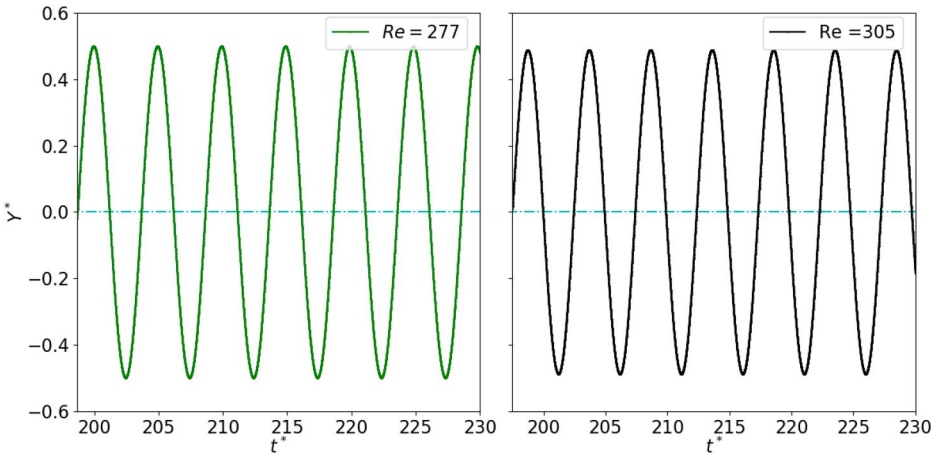


FIG. 4. The displacement history for $\zeta = 0, m^* = 10$, and $f^* = 0.20$ for $Re = 277$ and 305 to show the sinusoidal nature.

oscillating amplitude is a function of the reduced velocity, so by running simulations over a range of Reynolds numbers, the transition Reynolds number can be determined and the oscillation amplitude noted for a particular system frequency. The transition Reynolds number can then be compared with the published result of Leontini *et al.* (2007), under the assumption that the displacement variation is sinusoidal.

The predictions of Leontini *et al.* (2007) show that for a forced oscillation amplitude of $A^* = 0.5$, and forcing frequency $f^* = 0.2$, mode A^* becomes unstable at $Re_{c,A} \sim 305$ and mode B at $Re_{c,B} \simeq 277$. Thus, simulations were run for $Re = 277$ and 305 for $\zeta = 0, m^* = 10$ and $f^* = 0.20$ corresponding to the standard VIV spring-damping system. Note that in both cases the saturation amplitude reaches $A \simeq 0.50$. The displacement histories are presented in Fig. 4 to show the displacement signal, Y^* is close to sinusoidal for this case.

Figure 5 shows that at $Re = 277$, the maximum amplitude multiplier is close to unity for the solution branch corresponding to mode B, while for $Re = 305$, the maximum amplitude of the mode A branch also reaches a value close to unity. Both of these predictions are in close accord with those from the forced oscillation study of Leontini *et al.* (2007), validating the method for at least the standard spring–damper VIV system.

III. RESULTS

In this section, the stability of the wake to three-dimensional transition for the vortex-induced vibration for a circular cylinder on viscoelastic support is analyzed. First, we analyze an undamped cylinder for both $m^* = 10$ and 2.546 at $f^* = 0.2$, noting that the frequency of oscillation is close to that of a fixed cylinder for $Re \sim 200$. We discuss the occurrence of modes A, B, and QP as Re is increased. In the second part of the study, we determine the value of Re and wavelength, λ, for which the two-dimensional wake becomes linearly unstable for the periodic flow of a cylinder under VIV. The cylinder supported by an SLS spring–damper support has been calculated at three values of damping ratio, $\zeta = 0.001, 1, 10$ and $R = 1$. This study shows a non-monotonic variation of critical Re with a damping ratio.

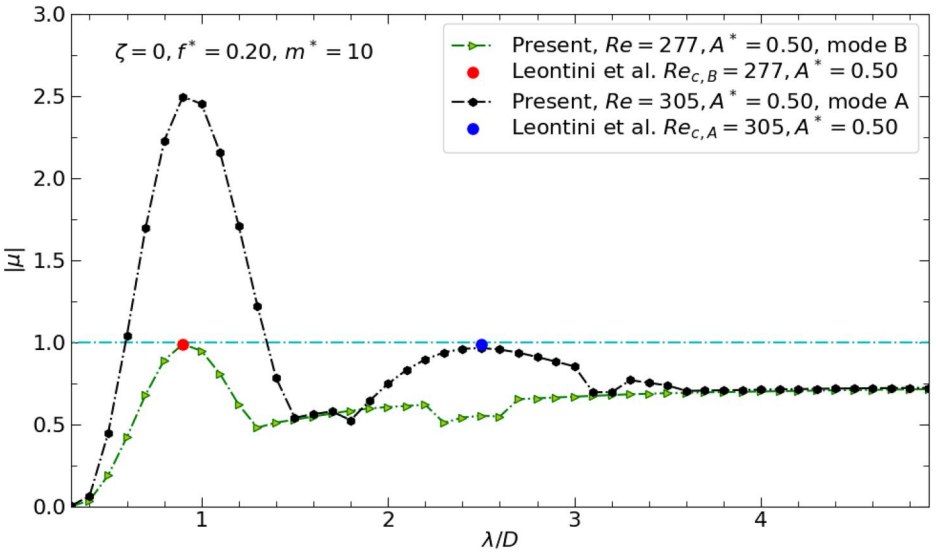


FIG. 5. Floquet multiplier vs spanwise wavelength at $Re = 277$ and 305, for $\zeta = 0$, $f^* = 0.20$, and $m^* = 10$, corresponding to a standard spring–damper VIV system. Mode B becomes critical first at $Re \simeq 277$ and then mode A for $Re = 305$.

22 June 2026 08:21:47

Published under an exclusive license by AIP Publishing

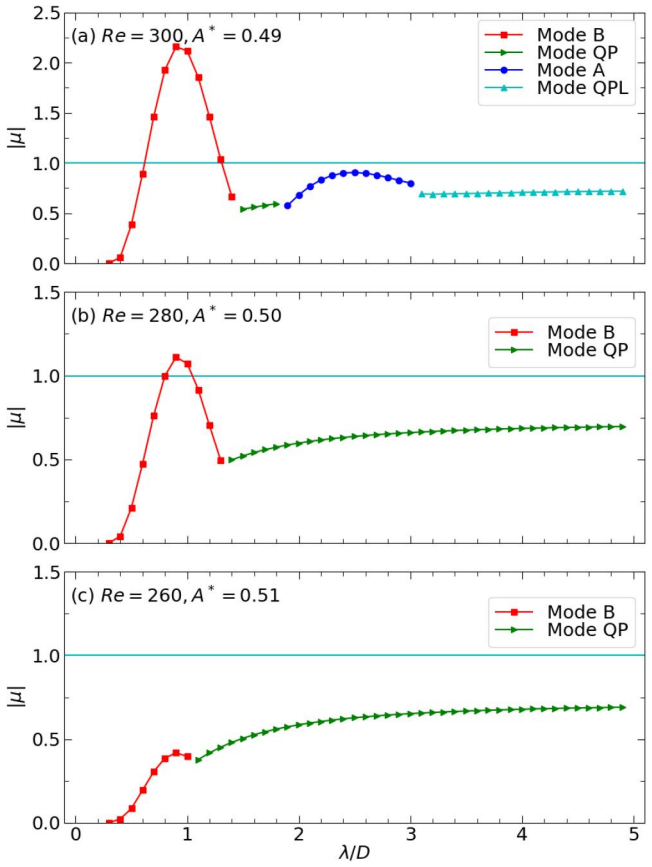


FIG. 6. Floquet multiplier versus wavelength at $Re = 300, 280$, and 260; $\zeta = 0$ (undamped system), $f^* = 0.20$, and $m^* = 10$.

A. Undamped VIV of a circular cylinder

Figure 6 shows the predicted Floquet multiplier amplitude, $|\mu|$, vs wavelength, λ, for undamped free vibration corresponding to a single spring elastic mounting with spring constant k. The frequency of oscillation is fixed at $f^* = 0.2$, close to the shedding frequency of the fixed cylinder. Three Reynolds numbers: $Re = 260, 280$, and 300, are analyzed for a mass ratio $m^* = 10$. The Reynolds numbers are chosen to cover the range of stable and unstable modes. Figure 6 clearly shows that for $Re = 300$ and 280, the flow is unstable to three-dimensional perturbations, whereas at $Re = 260$ the 2-D wake flow is stable ($|\mu| < 1$), with different modes observed. The amplitude of oscillation increases slightly with decreasing Re, with $A^* = 0.49$, 50, and 0.51, for $Re = 300, 280$, and 260, respectively. We observe that mode B is critical first then mode A; similar results were shown for $A^* > 0.3$ under forced cylinder oscillation by Leontini *et al.* (2007). In the case of $Re = 300$, only mode B is unstable with the maximum growth rate occurring at $\lambda \approx 0.9D$. Mode QP (quasi-periodic) with a complex Floquet multiplier remains stable and occurs over the range $1.4 < \lambda < 1.9D$. At $Re = 300$ mode A is also stable with a maximum $|\mu| \approx 0.9$ occurring at $\lambda \approx 2.5D$. For $\lambda > 3.7D$, we observe a complex Floquet multiplier that appears to correspond to a quasi-periodic mode. Since it is observed at a longer wavelength than mode A, and to make a clear distinction from the previously observed QP mode, it is designated as mode QPL, named for *long-wavelength* quasi-periodic. For $Re = 280$, flow is still unstable to mode B, again focused at $\lambda \approx 0.9D$, whereas mode QP remains stable and can be observed for $\lambda > 1.4D$. For $Re = 260$, mode B remains focused around $\lambda \approx 0.9D$ but is stable, and mode QP is found beyond $\lambda > 1.10D$. A clear distinction between mode QP and mode QPL is not seen for $Re = 260$ and 280.

Figure 7 shows the spanwise perturbation-vorticity fields at $Re = 300$ in order to quantitatively depict the structures of modes B and A. As illustrated in Fig. 7(a), mode B is the first mode to become unstable and attains the maximum $|\mu|$ at $\lambda \approx 0.9D$. The mode retains the spatio-temporal symmetry of the base flow about the wake centerline. In contrast to mode B, mode A remains stable and reaches its maximum $|\mu|$ at $\lambda \approx 2.5D$. This is shown in Fig. 7(b). Mode A has spatio-temporal symmetry opposite to that of mode B. The structures for modes A and B are found to be similar to those of modes A and B for a fixed circular cylinder (Barkley and Henderson, 1996). The time variation of modes QP and QPL are shown in Fig. 8. This shows a series of images of the perturbation field taken one base flow field period apart for $Re = 300$ at $\lambda = 1.9D$ and $3.7D$, characteristic λ for modes QP and QPL. The structure of mode QPL is similar to mode QP. However, considering the images at the same phase, the perturbation field seems to repeat over approximately three base periods, but the perturbation field grows or decays as time progresses.

The effect of mass ratio on Floquet stability analysis for VIV at $Re = 300$ is examined for mass ratios $m^* = 2.546$ and 10, in Fig. 9. The natural frequency of oscillation $f^* = 0.20$ is the same for both mass ratios. There is a slight increase in amplitude of vibration due to the decrease in mass ratio: $A^* = 0.49$ for $m^* = 10$, whereas $A^* = 0.50$ for $m^* = 2.546$. For both mass ratios the flow is unstable to mode B,

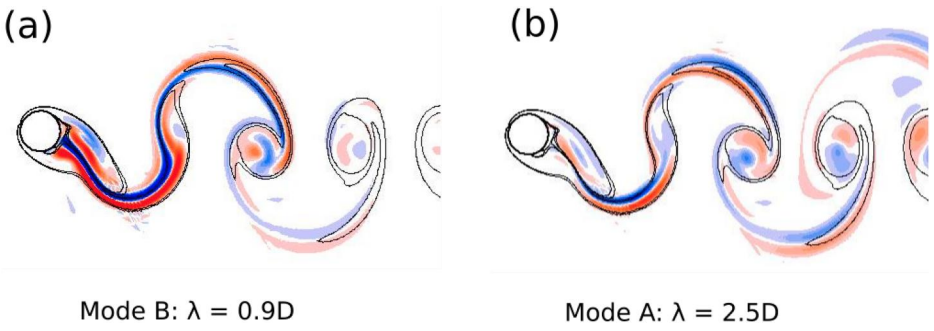


FIG. 7. Spanwise perturbation-vorticity depicting mode B (left) and A (right) at $Re = 300$, $\zeta = 0$, $f^* = 0.20$, and $m^* = 10$.

22 June 2026 08:21:47

Published under an exclusive license by AIP Publishing

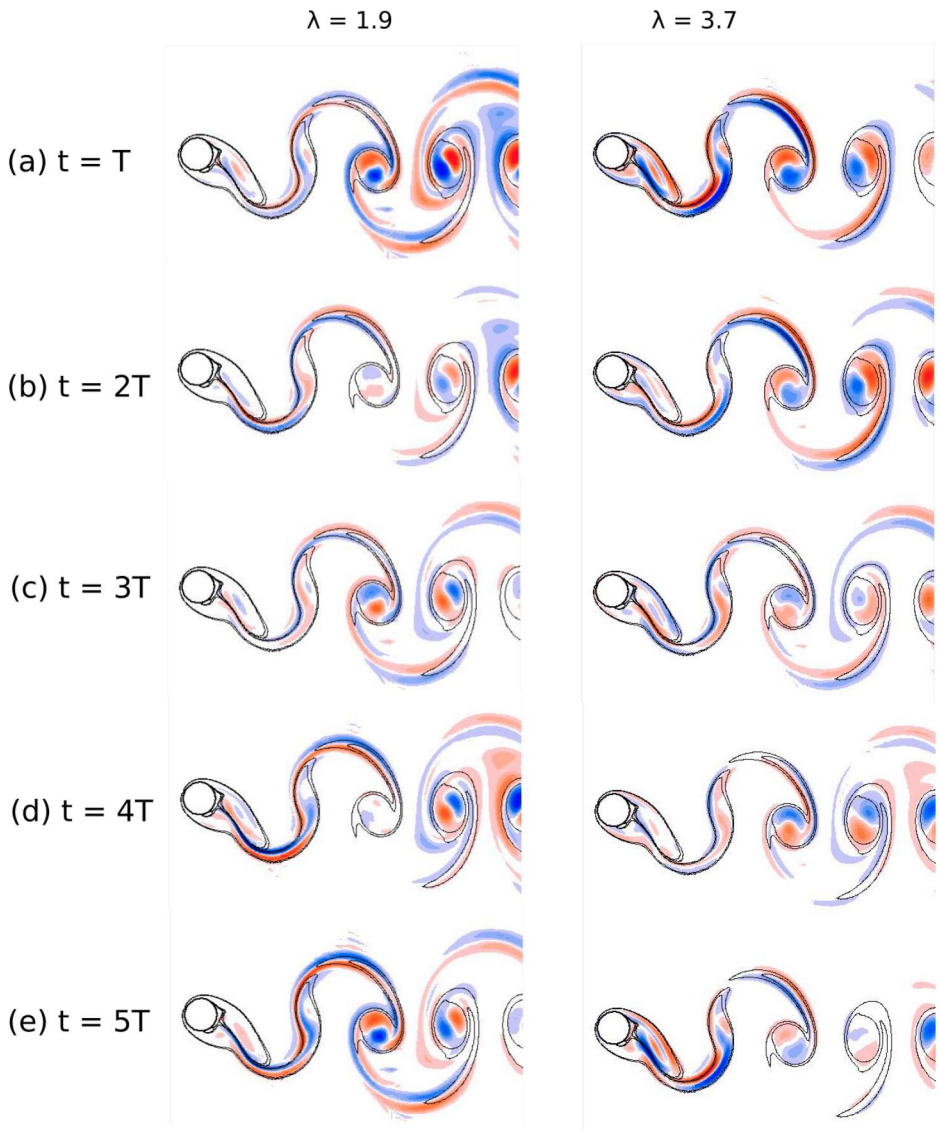


FIG. 8. Spanwise perturbation-vorticity fields representing modes QP (left) and QPL (right) at $Re = 300$, $\zeta = 0$, $f^* = 0.20$, and $m^* = 10$.

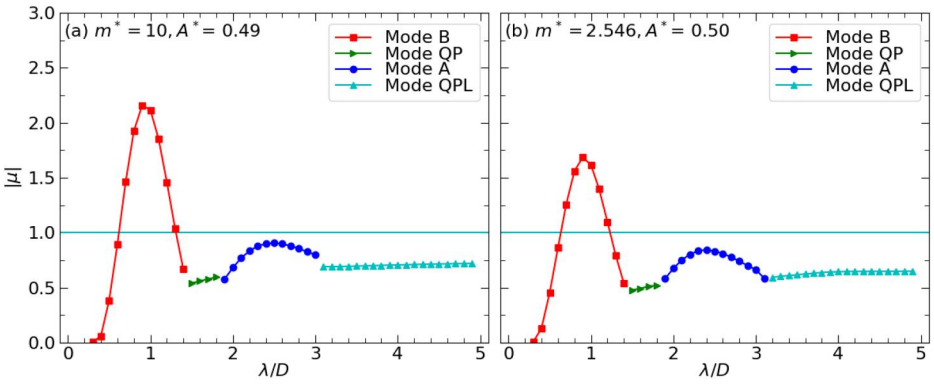


FIG. 9. Floquet multiplier versus wavelength for $m^* = 10$ (left) and 2.456 (right) at $Re = 300$, $\zeta = 0$, and $f^* = 0.20$.

22 June 2026 08:21:47

Published under an exclusive license by AIP Publishing

and the growth rate is higher for $m^* = 2.546$ than $m^* = 10$. All other modes, A, QP, and QPL, remain stable for both masses; however, the ranges of modes QP and A decrease at the lower m^*. The ranges dominated by QP and A for $m^* = 10$ are $1.5 \leq \lambda \leq 1.9D$ and $2.0D < \lambda < 3.6D$, whereas for $m^* = 2.546$ are $1.4D \leq \lambda \leq 1.5D$ and $1.6D \leq \lambda \leq 2.0D$. The maximum growth rate of each mode is also decreased from a maximum $|\mu| \approx 0.9$ to $|\mu| \approx 0.7$ with the decrease of mass ratio from 10 to 2.546. The effect of the mass ratio on three-dimensional stability under vortex-induced vibrations (VIV) at Re = 300 for mass ratios $m^* = 2.546$ and 10 in Fig. 9 shows that the response amplitude is approximately 0.49 in both cases. Furthermore, the dominant Floquet multiplier curves are virtually identical, despite the mass ratio being varied by a factor of four.

B. Comparison of variation of growth rate with damping ratio at *Re* = 300 for the SLS system

The standard linear solid system (SLS) is a nonstandard elastic mounting system, as shown in Fig. 1, consisting of two springs and a damper. Figure 10 illustrates the unstable modes at $Re = 300, U_r = 5$ on varying ζ. It shows the effect on wake transition and corresponding mode if damping is introduced to the undamped VIV, a classical VIV case. We can clearly see the amplitude of vibration A^* varies non-monotonically as ζ is varied; with $A^* = 0.49$ at $\zeta = 0$ decreasing to $A^* = 0.36$ at $\zeta = 1$, which further increases to $A^* = 0.48$ at $\zeta = 10$. This non-monotonic variation of A^* is due to the SLS structure model chosen and discussed in Mishra *et al.* (2020). For $\zeta = 0, 0.001$, and 10, mode B is unstable while other modes are stable; however, for $\zeta = 1$, modes B and A are both unstable. The possible reason may be due to the amplitude of vibration. The effect of amplitude on the criticality of all modes has been demonstrated by Leontini *et al.* (2007) for forced oscillation at reduced velocity $U_r = 5$. They have shown that for $A^* \approx 0.50$, the critical value for modes A and B are $Re \approx 305$ and $Re \approx 275$, respectively, whereas the critical values for modes A and B for $A^* \approx 0.36$ are $Re \approx 270$ and $Re \approx 275$, respectively. Clearly, for the case of $\zeta = 0, 0.001$, and 10, mode A becomes critical above $Re = 300$, and hence the mode is not unstable, whereas the opposite is true for mode B. Furthermore, for $\zeta = 1$, the critical value of Re is below $Re = 300$ for both modes A and B, indicating $|\mu| > 1$ (unstable) for both modes. In addition, for all damping ratios examined, mode B shows a maximum growth rate at $\lambda \approx 0.9D$. Mode A has maximum $|\mu|$ at $\lambda \approx 2.5D$ for $\zeta = 0, 0.001$, and 10; however, there is a slight increase in λ for $\zeta = 1$; the maximum growth rate occurs at $\lambda \approx 2.7D$. Leontini *et al.* (2007) have presented that the critical Re for QP is $Re \approx 305$ for an amplitude of vibration $A^* > 0.1$. This observation is in accord with the current findings, which show that modes QP and QPL are stable for $Re = 300$ as $|\mu|$ remains below $|\mu| = 1$.

The typical time-dependent dynamics of a Floquet mode are shown in Figs. 11 and 12. Figure 11 presents the evolution of the spanwise perturbation vorticity of mode A over one shedding cycle for $Re = 300, \zeta = 0.001, U_r = 5.0$, and $\lambda/D = 2.4$. The results show that the near-wake perturbation field initially develops within the nascent vortex cores and is especially strong in the highly strained developing braid region between these vortices, i.e., the stretched thin layer of vorticity connecting the main wake vortices. This is consistent with the near-wake perturbation field structure seen in mode A for a

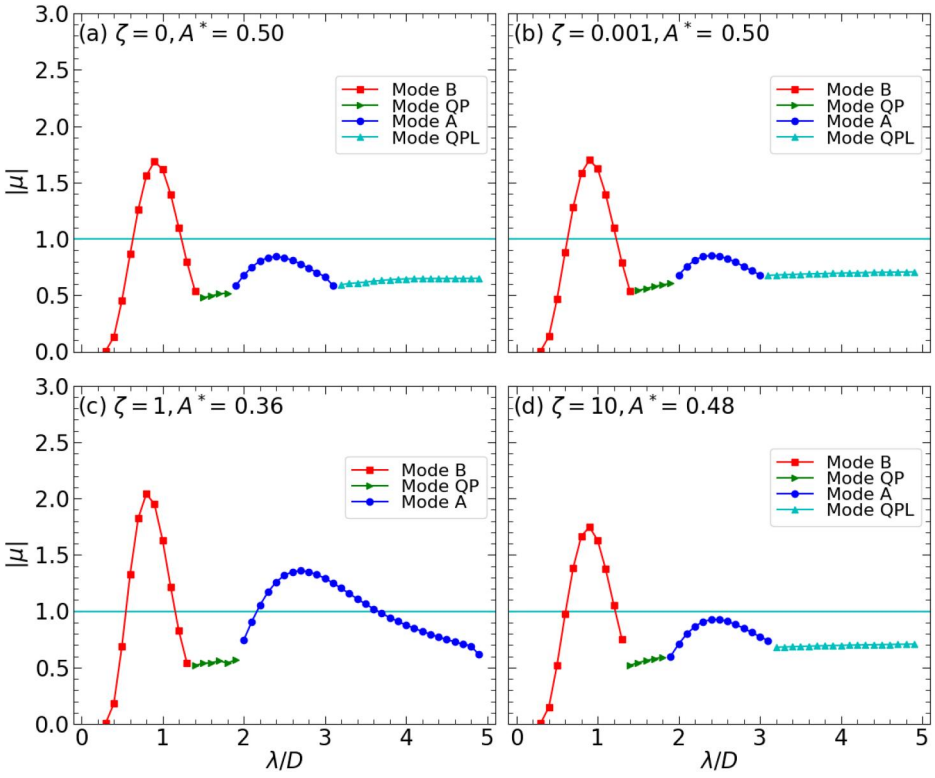


FIG. 10. Floquet multiplier versus wavelength at $U_r = 5$, $\zeta = 0, 0.001, 1$, and 10 for $m^* = 2.456$ and $Re = 300$.

22 June 2026 08:21:47

Published under an exclusive license by AIP Publishing

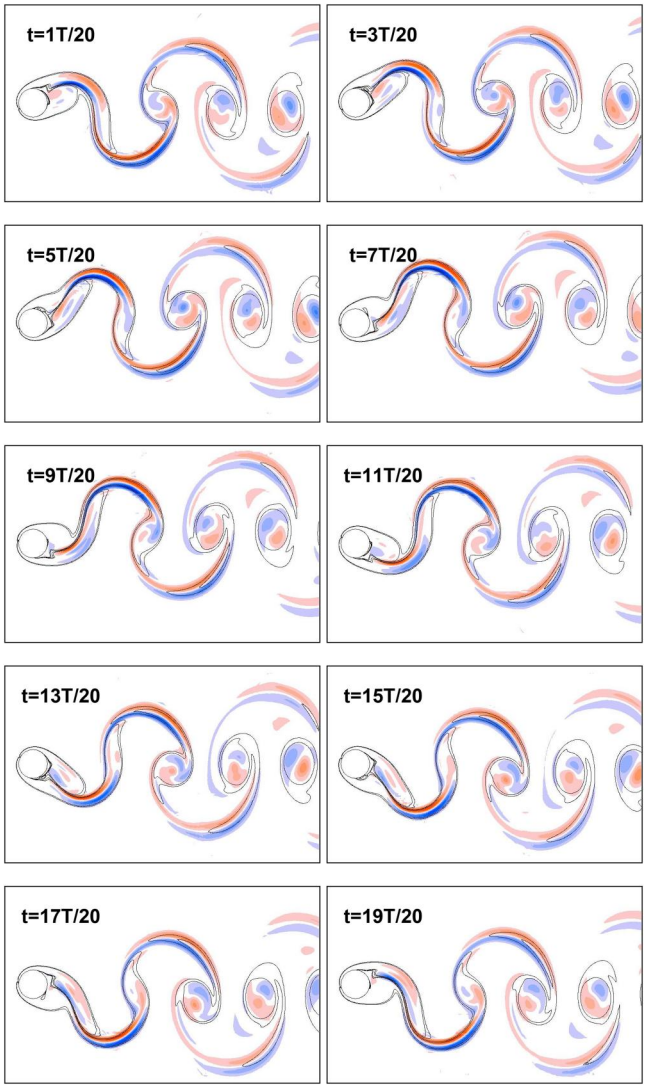


FIG. 11. Spanwise vorticity of mode A for $Re = 300, \zeta = 0.001$, and $U_r = 5.0$ at $\lambda/D = 2.4$. T is the period of oscillation.

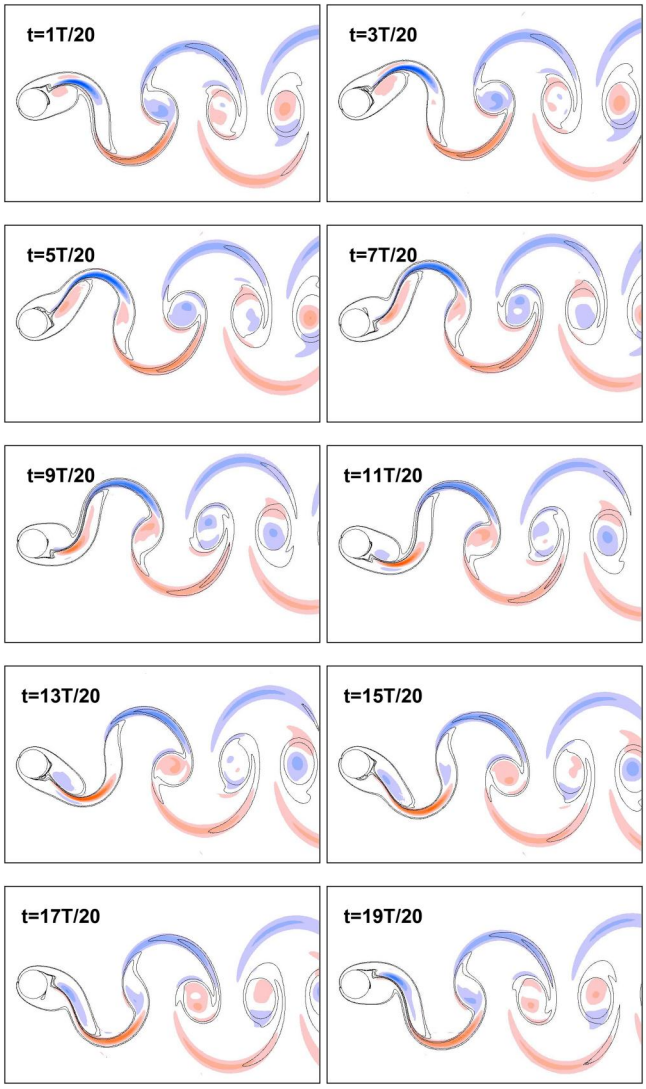


FIG. 12. Streamwise vorticity of mode A for $Re = 300, \zeta = 0.001$, and $U_r = 5.0$ at $\lambda/D = 2.4$. T is the period of oscillation.

stationary cylinder (e.g., see Barkley and Henderson, 1996; Thompson *et al.*, 2001). In this case, however, the newly formed vortices are more highly stretched as they are shed before again rolling up into more compact structures further downstream. As the braid region is advected downstream, the perturbation intensity increases rapidly at first before decreasing in strength even further downstream beyond the first two shed vortices. This is more pronounced than seen in the stationary cylinder wake, consistent with the less stretched braid region in that case. In the VIV case examined here, the stretching is stronger at least partially not only from the oscillation of the body but also from the higher Reynolds number than when mode A becomes critical for the stationary case ($Re \simeq 190$). In turn, this is also consistent with the lower preferred mode A wavelength than for the latter case: $2.4D$, reduced from $3.9D$, because of the relatively smaller length scale. Further downstream, the instability becomes strong in the vortex cores, with the perturbation spanwise vorticity showing the characteristic structure of elliptic instability, i.e., positive and negative lobes aligned at 45° to the semimajor axis of the elliptical cores, with the perturbation dropping to zero at the edge of the cores (Leweke and Williamson, 1998; Thompson *et al.*, 2001).

The evolution of the streamwise perturbation vorticity shown in Fig. 12 clearly demonstrates the spatio-temporal symmetry associated with mode A, with the streamwise vorticity reversing sign across the wake, or, alternatively, with the vorticity reversing sign every half-period. Mode B (not shown) in comparison shows streamwise perturbation vorticity of a single sign on both sides of the wake but swaps sign along the span of the cylinder. The streamwise perturbation vorticity is more concentrated in the braid regions than seen for mode A

22 June 2026 08:21:47

Published under an exclusive license by AIP Publishing

at onset for a stationary cylinder and is perhaps more reminiscent of the mode B spatial distribution. The stretching of the braid regions caused by VIV oscillations thus strongly affects the perturbation-vorticity spatial distribution and preferred wavelength while maintaining the spatio-temporal symmetry.

C. Effect of reduced velocity on different modes at $Re = 300$ for ζ=0.001 and 1

In Sec. III B, the stability analysis for VIV under SLS mounting has been performed for $U_r = 5$ at $Re = 300$ corresponding to the strongly resonate case. In this section, results for fixed $Re = 300$ at $\zeta = 0.001$ and $\zeta = 1$ are presented as a function of reduced velocity.

Figures 13 and 14 present $|\mu|$ as a function of λ for reduced velocities ranging from $U_r = 4.5$ to $U_r = 8$. These ranges are considered to satisfy the periodicity constraint for using Floquet stability analysis.

$U_r = 4.5$ for $\zeta = 0.001$ shows a subharmonic mode (SH), instead of mode A observed in all other cases beyond the QP mode. It is important to note that the Floquet multiplier in SH is always real and negative. For $\zeta = 0.001$, modes B, QP, and QPL are stable, whereas mode SH is marginally stable (critical) at $\lambda = 1.4D$. In contrast, for $\zeta = 1$, mode QP extends instead of mode SH, and is stable. For $\zeta = 0.001$, the SH mode is followed directly by the QPL mode, whereas for $\zeta = 1$, mode A is observed before the initiation of the QPL mode.

For $\zeta = 0.001$ at $U_r = 5$, mode A is observed for the first time but remains stable, whereas mode B is unstable. Interestingly, mode QPL is not observed for $\zeta = 1$; instead, mode A extends to $\lambda = 5D$ and is unstable.

For $\lambda < 5D$, mode QPL is observed only at $U_r = 4.5$ and 5 for $\zeta = 0.001$, and at $U_r = 4.5$ for $\zeta = 1$. However, mode QPL is absent at other reduced velocities, i.e., $U_r \in [5.5, 8]$.

It is observed that the stability of the modes is affected as U_r increases. Considering mode SH, which is observed only for $\zeta = 0.001$ at $U_r = 4.5$, the mode is marginally critical. Furthermore, mode QPL is observed at $U_r = 4.5$ and 5.0 for $\zeta = 0.001$, and at $U_r = 4.5$ for $\zeta = 1$.

Mode B is observed for all reduced velocities. It is stable at $U_r = 4.5$ but becomes unstable ($|\mu| > 1$) at higher reduced velocities, with $|\mu|$ increasing up to $U_r = 6.5$. For $U_r = 5.0$, the maximum value of $|\mu| \approx 1.7$ occurs at $\lambda \approx 0.9D$ for $\zeta = 0.001$, whereas for $\zeta = 1$, the maximum value of $|\mu| \approx 2.0$ occurs at $\lambda \approx 0.8D$. Upon further increasing U_r, the maximum value of $|\mu| \approx 4.0$ occurs at $\lambda \approx 1.0D$ for $U_r = 6.5$ for both $\zeta = 0.001$ and $\zeta = 1$. For $\zeta = 0.001$, the growth rate decreases at $U_r = 7$, with a maximum value of $|\mu| \approx 3.5$ occurring at $\lambda \approx 1.0D$. This value remains nearly constant with further increases in U_r. Specifically, the maximum $|\mu| \approx 3.5$ is observed at $\lambda \approx 1.0D$ for $U_r = 7$, 7.5, and 8. In contrast to $\zeta = 0.001$, the growth rate for $\zeta = 1$ increases slightly from $U_r = 6.5$ to $U_r = 7.0$. Furthermore, for $U_r = 7.5$ and 8.0, the growth rates are approximately the same for both $\zeta = 0.001$ and $\zeta = 1$.

Mode A observed to exist for all reduced velocities except for $\zeta = 0.001$ at $U_r = 4.5$. For $U_r = 5.0$ mode A is stable for $\zeta = 0.001$, whereas it is unstable for $\zeta = 1$ with the maximum $|\mu| \approx 1.4$ occurring at $\lambda \approx 2.7D$. Mode A observed to behave similarly to mode B for

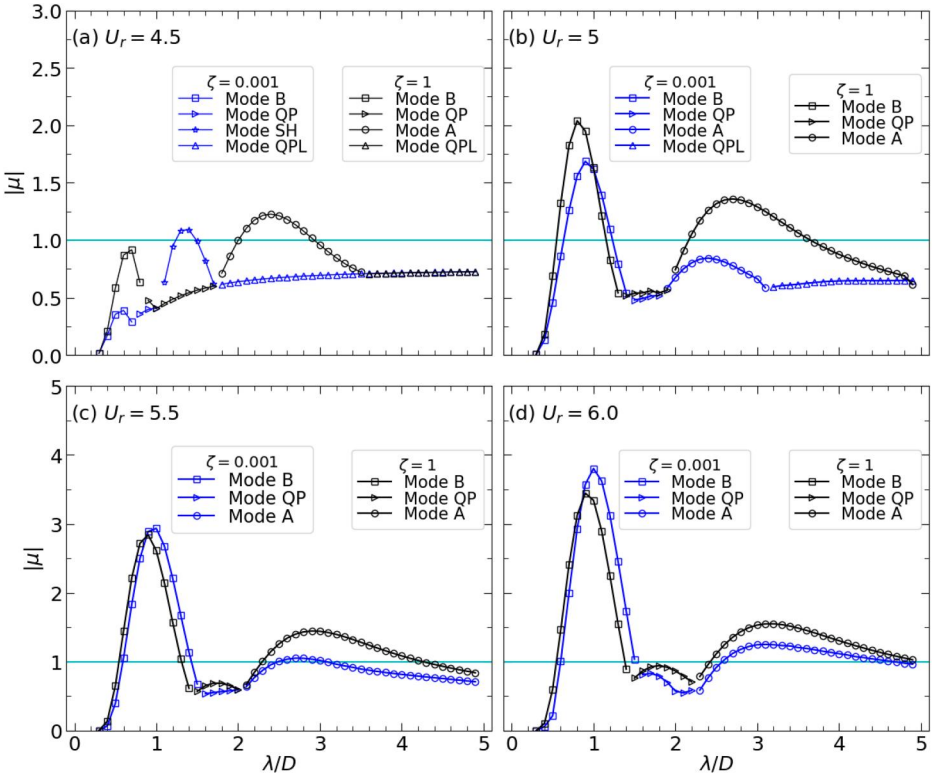


FIG. 13. Floquet multiplier versus wavelength, at $Re = 300$, $\zeta = 0.001$ and 1, $m^* = 2.546$ for (a) $U_r = 4.5$, (b) $U_r = 5.0$, (c) $U_r = 5.5$, and (d) $U_r = 6.0$.

22 June 2026 08:21:47

Published under an exclusive license by AIP Publishing

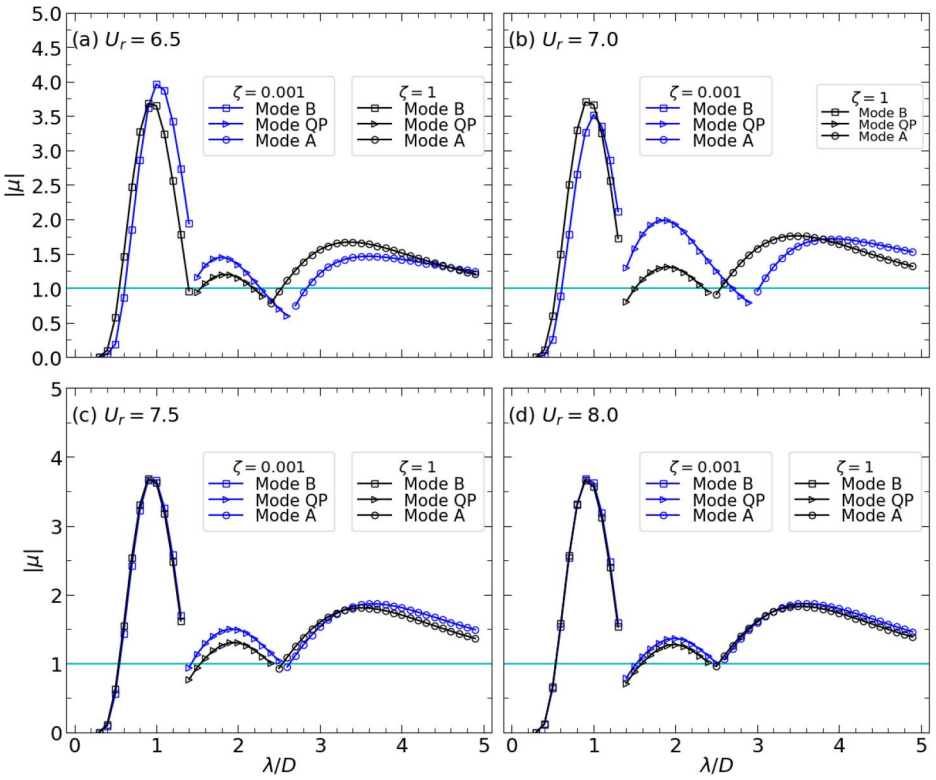


FIG. 14. Floquet multiplier versus wavelength, at $Re = 300$, $\zeta = 0.001$ and 1, $m^* = 2.546$ for (a) $U_r = 6.5$, (b) $U_r = 7.0$, (c) $U_r = 7.5$, and (d) $U_r = 8.0$.

$U_r > 5$. For $\zeta = 0.001$ at $U_r = 5.5$, the maximum $|\mu| \approx 1.03$ occurs at $\lambda \approx 2.7D$, indicating that the mode is just supercritical. However, for $\zeta = 1$, the system is unstable, with a maximum $|\mu| \approx 1.5$ occurring at $\lambda \approx 2.8D$. For both $\zeta = 0.001$ and $\zeta = 1$, the growth rate further increases with increasing U_r up to $U_r = 7.5$, reaching a maximum $|\mu| \approx 1.9$ at $\lambda \approx 3.6D$. Beyond $U_r \geq 7.5$, the growth rate for both $\zeta = 0.001$ and $\zeta = 1$ remains constant.

Mode QP is seen to exist for all reduced velocities in the range $U_r = [4.5, 8]$. For $\zeta = 0.001$ and 1, mode is stable for $U_r = [4, 5, 6.0]$. Interestingly, mode QP is critical at $U_r = 6.0$ for $\zeta = 1$. For $\zeta = 0.001$, the maximum $|\mu|$ increases up to $U_r = 7$, with a highest growth rate of $|\mu| \approx 1.9$ at $\lambda \approx 1.9D$. However, the growth rate for $\zeta = 1$, is lower with $|\mu| \approx 1.3$ at $\lambda \approx 1.9D$. On increasing U_r beyond 7.5, the maximum $|\mu|$ slightly decreases with a maximum of $|\mu| \approx 1.5$ for $\zeta = 0.001$ and $|\mu| \approx 1.3$ for $\zeta = 1$ at $U_r = 7.5$, centered around $\lambda = 1.9D$. At $U_r = 8.0$, growth rate further decreases with μ are approximately the same for $\zeta = 0.001$ and 1, having maximum $|\mu| \approx 1.3$ at $\lambda \approx 1.9D$.

D. Variation of the critical *Re* and wavelength for the standard linear solid (SLS) VIV system

In this section, maximum *Re* for which the wake remains two-dimensional is presented for the standard linear solid (SLS) VIV system as a function of reduced velocity, U_r.

Figure 15 presents the critical Reynolds number, Re_{cr}, and the corresponding critical wavelength, λ_{cr}, as functions of the reduced velocity, U_r, for undamped system. The critical Reynolds number, Re_{cr}, is defined as the Reynolds number at which a given mode first becomes unstable, i.e., when the growth rate first exceeds unity ($|\mu| > 1$). The corresponding critical wavelength, λ_{cr}, is the wavelength at which Re_{cr} occurs.

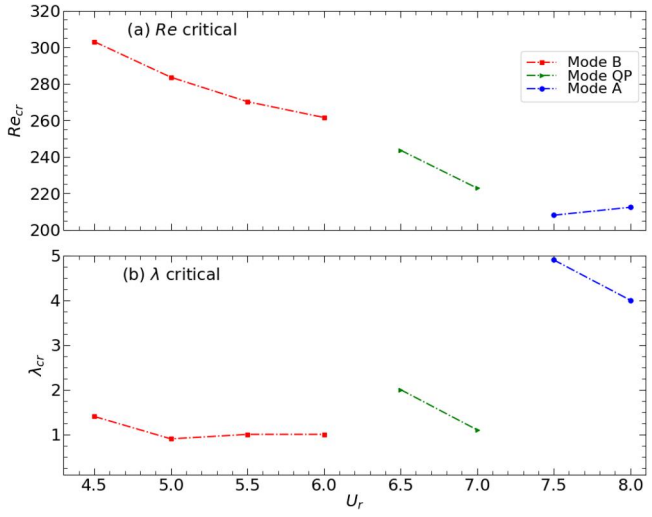


FIG. 15. Critical Reynolds Re_{cr} and critical wavelength λ_{cr} vs reduced velocity for undamped system at $U_r = [4.5, 8]$, $m^* = 2.546$.

To accurately determine Re_{cr} for each value of U_r, simulations were performed over a range of Reynolds numbers, with each *Re*

22 June 2026 08:21:47

Published under an exclusive license by AIP Publishing

evaluated for a series of wavelengths, λ, in increments of 0.1. For a given Reynolds number, the variation of $|\mu|$ with λ exhibits a quadratic trend in the vicinity of each local maximum, as demonstrated in the earlier $|\mu|$ vs λ plots. The coordinates of each local maximum, $(|\mu|, \lambda)$, were identified, and the Reynolds number was subsequently increased in increments of 5. At each increment, the maximum value of $|\mu|$ and its corresponding wavelength were recorded. This procedure was repeated until values yielding a maximum Floquet multiplier, $|\mu| = 1$ were resolved. The critical Reynolds number, Re_{cr}, was then determined through quadratic interpolation of the Reynolds number and the corresponding maximum values of $|\mu|$. An identical procedure was followed for each reduced velocity, U_r.

Figure 15(a) shows the variation of Re_{cr} with reduced velocity U_r. The critical Reynolds number, Re_{cr}, decreases with reduced velocity over the range of $U_r = [4.5, 7.0]$ considered. $Re_{cr} \approx 303$ at $U_r = 4.5$ decreases to $Re_{cr} \approx 212$ at $U_r = 8.0$. It is observed that for $U_r = [4.5, 6.0]$, the onset of mode B becomes critical first, whereas for $U_r = [6.5, 7.0]$ mode QP is critical first. For $U_r = [7.5, 8.0]$, mode A precedes the occurrence of the other modes. The decrease of the amplitude of oscillation, A^*, may be the cause of a decrease in Re_{cr} with U_r and the observed criticality of the modes. For $U_r = [4.5, 6.0]$, A^* decreases approximately from 0.52 to 0.45 with U_r, whereas for $U_r = [7.5, 8.0]$, $A^* \approx 0.11$. These findings are in accordance with Leontini *et al.* (2007) for the forced oscillation case: for $A^* < 0.3$, mode A was found to be critical; while for $A^* > 0.3$ mode B was critical. It is also observed that for $U_r = 6.5, 7$, mode QP first becomes critical, which is different from Leontini *et al.* (2007). The difference may be due to the difference in the frequency of oscillation.

Figure 15(b) shows the variation of λ_{cr} with reduced velocity U_r. The values of λ_{cr} presented show that λ_{cr}, for $U_r = 4.5$ to 5.0, decreases slightly from $\lambda_{cr} \approx 1.4D$ to $0.9D$; however, further increasing $U_r = 5.0$ to 6.0 results in $\lambda_{cr} \approx 0.9D$ unchanged for mode B. Furthermore, for mode QP for $U_r = 6.6$ and 7, $\lambda_{cr} \approx 2.0D$, reducing to $1.0D$. For $U_r = 7.5$ and 8, λ_{cr} decreases from $\lambda_{cr} = 4.9D$ to $4.0D$, with increasing U_r.

The standard VIV (undamped) system is extended for SLS VIV system to compare the 3D transition effects when SLS viscoelasticity is introduced. Results are presented for $\zeta = 0.001$and1 for a reduced velocity in the range $U_r = [4.5, 8]$, to depict the critical Reynolds number, Re_{cr} for which the flow remains two-dimensional. Figure 16 shows the critical Reynolds number, Re_{cr}, and corresponding critical wavelength, λ_{cr}, vs U_r.

Figure 16(a) shows the variation of Re_{cr} and λ_{cr} with reduced velocity U_r for $\zeta = 0.001$ is similar to the undamped system. The critical Reynolds number, Re_{cr}, decreases with reduced velocity over the entire range of U_r considered. For example, $Re_{cr} \approx 300$ at $U_r = 4.5$ decreases to $Re_{cr} \approx 260$ at $U_r = 6.0$. It further decreases to $Re_{cr} \approx 243$ at $U_r = 6.5$ reducing to $Re_{cr} \approx 212$ at $U_r = 8.0$. The onset of modes is also same. This change in the Re_{cr} and λ_{cr} reflects the changes in the base flow shown in Fig. 17. With increasing U_r from 4.5 to 8, Re_{cr} decreases, allowing the flow to remain attached for longer. This in turn reduces the wake width and the lateral spacing between vortices [see Figs. 17(g) and 17(h)] and influences the sudden increase in λ_{cr}.

Figure 16(b) shows the variation of Re_{cr} and λ_{cr} for $\zeta = 1$. The critical Reynolds number, Re_{cr}, decreases with reduced velocity similar to undamped and $\zeta = 0.001$. It can be observed that for $\zeta = 1$, the critical Reynolds numbers are lower than the corresponding $\zeta = 0$ (undamped) and $\zeta = 0.001$ (SLS) cases. The critical Reynolds number, $Re_{cr} \approx 285$ at $U_r = 4.5$ decreases to $Re_{cr} \approx 255$ at $U_r = 6.0$. It further decreases to $Re_{cr} \approx 226$ at $U_r = 6.5$, which increases slightly to $Re_{cr} \approx 230$ at $U_r = 7.0$. Further increasing the U_r, Re_{cr} decreases to $Re_{cr} \approx 223$ at $U_r = 7.5$ to $Re_{cr} \approx 218$ at $U_r = 8.0$. The transition modes are the same as observed for undamped and $\zeta = 0.001$, except at $U_r = 4.5$ and 8.0, which shows A and QPL transition modes, respectively. The possible explanation for the decrease in Re_{cr} is the decrease in amplitude. For $U_r = [4.5, 6.5]$, A^* decreases approximately from 0.38 to 0.20 with U_r, whereas for $U_r = [7.0, 8.0]$, A^* decreases approximately from 0.16 to 0.12. The variation of λ_{cr} with U_r at $\zeta = 1$ is different from $\zeta = 0.001$. At $U_r = 4.5$, the mode A transition occurs at $\lambda_{cr} = 2.4D$, which decreases to $\lambda_{cr} = 0.8D$ for $U_r = 5$. The λ_{cr} remains constant for $U_r = [5.5, 6.0]$, $U_r = [6.5, 7.0]$, and $U_r = [7.5, 8.0]$ with corresponding values as $\lambda_{cr} = 0.9D$, $2.0D$, and $3.9D$, respectively.

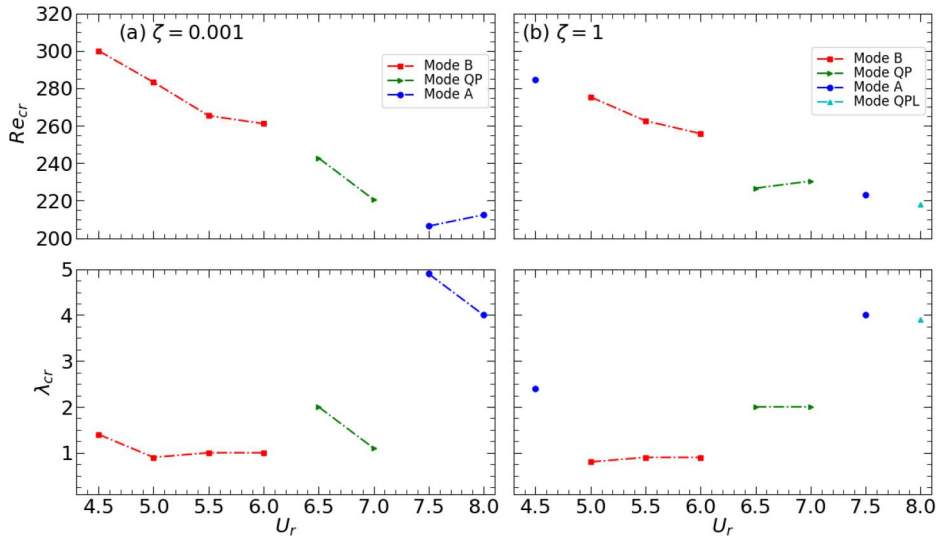


FIG. 16. Critical Reynolds Re_{cr} and critical wavelength λ_{cr} vs reduced velocity for $\zeta = 0.001, 1$ corresponding to $U_r = [4.5, 8], m^* = 2.546$.

22 June 2026 08:21:47

Published under an exclusive license by AIP Publishing

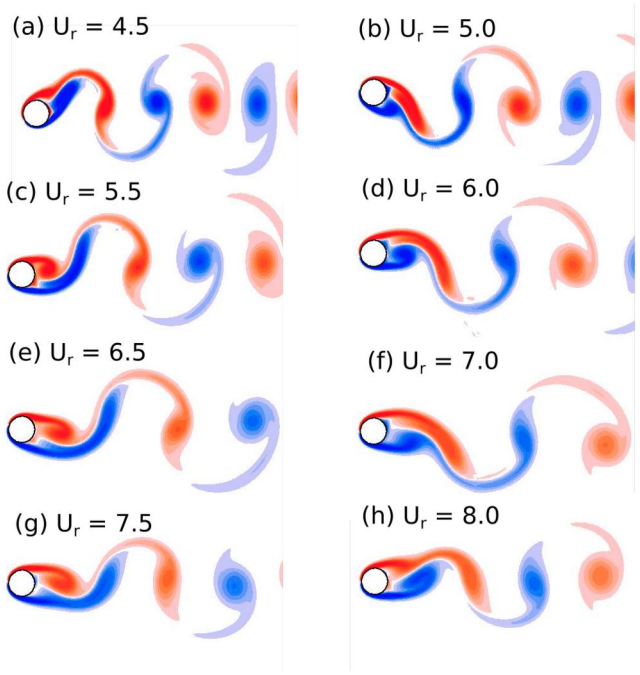


FIG. 17. Base flow vorticity contour at critical Re for $U_r = [4.5, 8]$ at $\zeta = 0.001, m^* = 2.546$.

For both, the standard spring–damper and SLS VIV system, the maximum Re for which the wake remains two-dimensional is 212 and occurs at $U_r = 8$, corresponding to a critical lambda of $\lambda_{cr} \approx 4.0D$. The maximum delay in transition from two- to three-dimensional flow occurs for $U_r = 4.5$, with the wake remaining 2D up to $Re_{cr} \approx 303$, 300, and 285 for the undamped case and $\zeta = 0.001$and1, respectively.

Overall, the results demonstrate that the oscillation amplitude plays a significant role in preserving the two-dimensional character of the wake. Specifically, large-amplitude transverse oscillations significantly delay the onset of the three-dimensional transition. This delay is attributed to the establishment of a strong lock-in regime, wherein the vortex shedding frequency synchronizes with the imposed cylinder oscillation. Such synchronization enforces phase coherence in the wake dynamics, thereby suppressing the growth of spanwise perturbations and stabilizing the two-dimensional base flow over an extended Reynolds number range. Consequently, the critical Reynolds number for the onset of secondary (3D) instability is shifted to higher values under high-amplitude forcing.

IV. CONCLUSIONS

A Floquet stability analysis of flow past a circular cylinder undergoing VIV subject to a standard linear solid (SLS) viscoelastic support has been undertaken. For the damping ratio $\zeta = 0$, it corresponds to an standard spring VIV system. It is found that for $Re = 300$, modes A, B, and QP can be observed, with the initial three-dimensional transition through mode B at $\lambda \approx 0.9D$. The 3D onset mode changes from mode B to mode A via mode QP as λ is increased. Under SLS support, as the ζ is increased from 0 to 10, we observe a non-monotonic variation of amplitude response. This, in turn, affects the wake instability. We observe at $Re = 300$, mode B is unstable for $\zeta = 0, 0.001$, and 10, whereas mode A is only unstable for $\zeta = 1$.

The $\zeta = 0.001$ and $\zeta = 1$ case is investigated for reduced velocity in the range $U_r = [4.5, 8]$ at $Re = 300$. It is found that mode B is unstable for all cases except for $U_r = 4.5$. Interestingly, for $U_r = 4.5$, the subharmonic (SH) mode is observed only for $\zeta = 0.001$, and is found to be the critical mode. In all other cases, mode A is observed instead of SH mode. This may be due to the high amplitude and low frequency of oscillation as compared to the other reduced velocities. The critical Re for three-dimensional transition has been observed to decrease as U_r increases from 4.5 to 8.

Thus, the transition of the wake from two-dimensional to three-dimensional flow is found to be governed by modes A, B, QP, and SH, with their occurrence dependent on the oscillation amplitude and reduced velocity. The maximum Re for which the wake remains two-dimensional for $U_r = [4.5, 8]$, is 212. The results may be helpful for guidance with three-dimensional numerical investigations of VIV under viscoelastic support subject to the careful tuning of the damping ratio ζ.

ACKNOWLEDGMENTS

This work was supported by computational resources provided by the National Computational Infrastructure and Pawsey Supercomputer Centre (NCMAS Merit Grant d71) under the National Computational Merit Allocation Scheme.

AUTHOR DECLARATIONS

Conflict of Interest

The authors have no conflicts to disclose.

Author Contributions

Rahul Mishra: Conceptualization (equal); Data curation (equal); Formal analysis (equal); Investigation (equal); Methodology (equal); Software (equal); Validation (equal); Visualization (equal); Writing – original draft (equal); Writing – review & editing (equal). **Rajneesh Bhardwaj:** Conceptualization (equal); Data curation (equal); Investigation (equal); Methodology (equal); Project administration (equal); Supervision (equal); Visualization (equal); Writing – original draft (equal); Writing – review & editing (equal). **Mark C. Thompson:** Conceptualization (equal); Data curation (equal); Formal analysis (equal); Funding acquisition (equal); Investigation (equal); Methodology (equal); Project administration (equal); Resources (equal); Software (equal); Supervision (equal); Validation (equal); Visualization (equal); Writing – original draft (equal); Writing – review & editing (equal).

DATA AVAILABILITY

The data that support the findings of this study are available from the corresponding author upon reasonable request.

REFERENCES

Barkley, D. and Henderson, R. D., "Three-dimensional Floquet stability analysis of the wake of a circular cylinder," J. Fluid Mech. **322**, 215–241 (1996).

22 June 2026 08:21:47

Published under an exclusive license by AIP Publishing

Bearman, P. W., "Vortex shedding from oscillating bluff bodies," Annu. Rev. Fluid Mech. **16**, 195–222 (1984).
Bearman, P. W., "Circular cylinder wakes and vortex-induced vibrations," J. Fluids Struct. **27**, 648–658 (2011).
Blackburn, H. M. and Lopez, J. M., "On three-dimensional quasiperiodic Floquet instabilities of two-dimensional bluff body wakes," Phys. Fluids **15**, L57–L60 (2003).
Eswaran, M., Sajish, S., and Natesan, K., "Investigation of flow-induced vibration in core sub-assemblies of sodium-cooled fast reactors," Prog. Nucl. Energy **185**, 105780 (2025).
Hourigan, K., Thompson, M. C., and Tan, B. T., "Self-sustained oscillations in flows around long blunt plates," J. Fluids Struct. **15**, 387–398 (2001).
Karniadakis, G. and Sherwin, S., *Spectral/hp Element Methods for Computational Fluid Dynamics* (Oxford University Press, 2013).
Karniadakis, G. E., Israeli, M., and Orszag, S. A., "High-order splitting methods for the incompressible Navier-Stokes equations," J. Comput. Phys. **97**, 414–443 (1991).
Leontini, J., Thompson, M., and Hourigan, K., "The beginning of branching behaviour of vortex-induced vibration during two-dimensional flow," J. Fluids Struct. **22**, 857–864 (2006).
Leontini, J. S., Thompson, M. C., and Hourigan, K., "Three-dimensional transition in the wake of a transversely oscillating cylinder," J. Fluid Mech. **577**, 79–104 (2007).
Leweke, T. and Williamson, C. H. K., "Three-dimensional instabilities in wake transition," Eur. J. Mech.-B/Fluids **17**, 571–586 (1998).
Mishra, R., Bhardwaj, R., Kulkarni, S. S., and Thompson, M. C., "Vortex-induced vibration of a circular cylinder on a nonlinear viscoelastic support," J. Fluids Struct. **100**, 103196 (2021).
Mishra, R., Bhardwaj, R., and Thompson, M. C., "Three-dimensional transition of the flow past an elastically mounted circular cylinder," J. Fluid Mech. **984**, A12 (2024).
Mishra, R., Kulkarni, S. S., Bhardwaj, R., and Thompson, M. C., "Response of a linear viscoelastic splitter plate attached to a cylinder in laminar flow," J. Fluids Struct. **87**, 284–301 (2019).
Mishra, R., Soti, A., Bhardwaj, R., Kulkarni, S. S., and Thompson, M. C., "Transverse vortex-induced vibration of a circular cylinder on a viscoelastic support at low Reynolds number," J. Fluids Struct. **95**, 102997 (2020).
Parkinson, G., "Phenomena and modelling of flow-induced vibrations of bluff bodies," Prog. Aerosp. Sci. **26**, 169–224 (1989).
Rajamuni, M. M., Thompson, M. C., and Hourigan, K., "Transverse flow-induced vibrations of a sphere," J. Fluid Mech. **837**, 931–966 (2018).
Rao, A., Radi, A., Leontini, J. S., Thompson, M. C., Sheridan, J., and Hourigan, K., "A review of rotating cylinder wake transitions," J. Fluids Struct. **53**, 2–14 (2015).
Ryan, K., Thompson, M. C., and Hourigan, K., "Three-dimensional transition in the wake of bluff elongated cylinders," J. Fluid Mech. **538**, 1–29 (2005).
Sarpkaya, T., "Vortex-induced oscillations: A selective review," J. Appl. Mech. **46**, 241–258 (1979).
Sarpkaya, T., "A critical review of the intrinsic nature of vortex-induced vibrations," J. Fluids Struct. **19**, 389–447 (2004).
Sheard, G. J., Thompson, M. C., and Hourigan, K., "From spheres to circular cylinders: The stability and flow structures of bluff ring wakes," J. Fluid Mech. **492**, 147–180 (2003).
Sheard, G. J., Thompson, M. C., and Hourigan, K., "Subharmonic mechanism of the mode C instability," Phys. Fluids **17**, 111702 (2005).
Soti, A. K., Zhao, J., Thompson, M. C., Sheridan, J., and Bhardwaj, R., "Damping effects on vortex-induced vibration of a circular cylinder and implications for power extraction," J. Fluids Struct. **81**, 289–308 (2018).
Thompson, M. C., Hourigan, K., Cheung, A., and Leweke, T., "Hydrodynamics of a particle impact on a wall," Appl. Math. Modell. **30**, 1356–1369 (2006).
Thompson, M. C., Hourigan, K., and Sheridan, J., "Three-dimensional instabilities in the wake of a circular cylinder," Exp. Therm. Fluid Sci. **12**, 190–196 (1996).
Thompson, M. C., Leweke, T., and Williamson, C. H. K., "The physical mechanism of transition in bluff body wakes," J. Fluids Struct. **15**, 607–616 (2001).
Williamson, C. H. K., "Vortex dynamics in the cylinder wake," Annu. Rev. Fluid Mech. **28**, 477–539 (1996).
Williamson, C. H. K. and Govardhan, R., "Vortex-induced vibrations," Annu. Rev. Fluid Mech. **36**, 413–455 (2004).
Williamson, C. H. K. and Govardhan, R., "A brief review of recent results in vortex-induced vibrations," J. Wind Eng. Ind. Aerodyn. **96**, 713–735 (2008).
Wu, X., Ge, F., and Hong, Y., "A review of recent studies on vortex-induced vibrations of long slender cylinders," J. Fluids Struct. **28**, 292–308 (2012).
Zhao, H., Yin, Y., Gao, P., Tian, R., Li, X., and Tan, S., "Numerical studies on the effect of surface roughness on flow field and flow-induced vibration in the in-line tube bundle," Nucl. Eng. Des. **424**, 113313 (2024).

22 June 2026 08:21:47

Published under an exclusive license by AIP Publishing